Full length article

Laser surface melting of Mg-Zn-Dy alloy for better wettability and corrosion resistance for biodegradable implant applications

Rakesh K.R.[a], Srikanth Bontha[a,*], Ramesh M.R.[a], Mitun Das[b], Vamsi Krishna Balla[b,*]

[a] Department of mechanical Engineering, National Institute of Technology Karnataka, Surathkal 575025, India
[b] Bioceramics and Coating Division, CSIR-Central Glass and Ceramic Research Institute, 196 Raja S.C. Mullick Road, Kolkata 700 032, West Bengal, India

ABSTRACT

In order to improve the performance of magnesium (Mg) for resorbable implant applications, Mg-1Zn-2Dy alloy was developed and the surface of the alloy has been modified by melting using lasers. Laser melted samples, at different laser energy density, were then subjected to microstructural, hardness, wettability and *in-vitro* degradation assessment. The microstructure of the Mg-Zn-Dy alloy mainly consisted of α-Mg and eutectic phase (Mg_8ZnDy). The melted region of the alloy surface evolved with fine grain microstructure at the near surface region and columnar grains near to the liquid solid substrate. The degree of grain size refinement obtained at the melted zone in the order of 1–2 μm. The cross sectional microhardness of the modified zone was measured by Vickers microhardness tester. Due to these microstructural refinements and solid solution strengthening the surface hardness of laser treated alloy increased by two-fold. It was found that as the energy density increased the surface roughness along with the surface energy also increased. The wetting behaviour of the surface was estimated through measuring the contact angle by dropping the polar and non-polar liquid. Results showed that the surface energy is also found to change with LSM due to changes in the surface morphology, microstructure and chemical composition of the material. The detailed degradation study was carried out by immersing the samples in hanks balances salt solution (HBSS).The improvement in the degradation behaviour followed by laser surface melting is related to the microstructural refinement as a result of rapid heating and cooling of the melted zone.

1. Introduction

In view of ideal temporary implant material, magnesium (Mg) and its alloys are potential candidates because of their biocompatibility and biodegradation properties. Compared with traditional implant materials such as titanium alloys, steel, polymers and ceramics the mechanical properties matches with the human bone there by avoiding stress shielding effects [1]. Mg is also a vital element to the human metabolism and Mg alloys can degrade in the physiological environment without releasing any toxic metallic ions. The corrosion properties of Mg alloys have to be carefully taken in to consideration to develop biodegradable Mg based implants. Often, Mg-based alloys are very active and exhibit rapid corrosion [2], which can result in premature failure of the implants [3]. However, improvements in the mechanical properties and corrosion resistance can be achieved by cautious alloying and surface modification techniques. On alloying aspects, progress on biomedical Mg alloys mainly happened on Mg-Zn-based [4], Mg-Ca-based [5], Mg-Zr based [6] and Mg-Zn-rare earth element (REE)

based alloys [7,8]. Among these, most of the *in-vivo* studies have been found to use REE alloys due to their strength and improved corrosion resistance. Out of all REE there are only few elements that were proven as an alloying element for biomedical application. In that aspect high solid solubility (25.3 wt% in Mg) dysprosium (Dy) element containing Mg alloys researched in the direction of *in vitro* cytotoxicity and it is proven to be more suitable with less toxicity than yttrium (Y) for biomedical application [8]. When dysprosium is alloying with magnesium and zinc, different types of strengthening structure known as long period stacking ordered phase (LPSO) formed and it is attributed with significant plasticity and toughness [9,10].

In order to tailor the corrosion behaviour and bioactivity of the alloy, the surface properties such as microstructure, surface morphology and near surface chemical compositions can be changed which can be achieved through different surface modification techniques. Conversion coating, deposited coating, friction stir processing and chemical passivation are some of the techniques deployed for surface modification of Mg alloys [11,12]. Among all, laser processing is a

captivating alternative for modifying surfaces through melting by high intensity laser beam. Through laser surface melting (LSM), comparatively refined and uniform microstructures with increased homogeneity were obtained due to rapid resolidification confined region to the surface [13]. AM60B magnesium alloy was surface melted using 10 kW CO_2 laser and results showed that homogenous distribution of β-phase with refined grains at the modified surface [14]. Laser melting also caused selective evaporation of Mg and Zn, and enrichment of Al leading to chemical compositional changes in the LSM regions. Such microstructural transition leads to superior corrosion resistance in the LSM modified layer [14]. Similarly AZ31, WE43 and AZ61 alloys reported to have improved corrosion resistance after laser surface melting using continuous CO_2 laser [15]. Taltavull et.al [16] used high power laser on AZ91D alloy and observed correlation between laser processing parameters and corrosion. It is concluded that at high laser power and low scan speed condition resulted in enhanced corrosion resistance. Resistance to pitting corrosion and microhardness of rare earth based Mg alloy MEZ (Zn-0.5% Mn-0.1%, Zr-0.1% REE 2% and remaining Mg) were also found to be improved by LSM treatment [17].

Successfully engineered surfaces of bio implants should functionally responsible for better protein absorption and cell harvesting under the biological environment [18]. In this contest surface parameters such as roughness, wettability, hydrophilicity/hydrophobicity and surface energy were found to be very critical for adhesion of cells on bone implant interface. The surface wettability can be efficiently tailored by laser surface modification techniques [19,20]. It was studied the changes in surface characteristics of laser surface nitride Ti-6Al-4V alloy. It is observed that at different energy densities the adhesion and viability of cells significantly modulated. Also, cell proliferation studies show that surfaces with higher roughness improved the cell adhesion [21] after laser based nitridation process. It is also concluded changes in surface chemical composition played a vital role in cell adhesion on the surface [22]. Demir et al. [23] used pulsed fiber laser on AZ31B (Mg alloy) for creating different surface structures (varying surface roughness) and studied for wettability. The result showed better control of the water contact angle with respect to the surface roughness. The main contribution of the wettability in this study is due to the increase in the real surface as a function of the surface roughness.

Till date, relatively handful studies have been carried out on the surface modification of Mg based rare earth element alloys using laser surface melting. Therefore, in the current study we aim to understand the influence of laser surface melting of in house developed Mg-1Zn-2Dy (wt%) alloy on microstructural changes, hardness variation, wettability behaviour and degradation resistance. Varying laser energy densities have been used to alter the surface characteristics of the alloy and proper co-relations have been drawn with respect to the untreated surface.

2. Materials and methods

2.1. Alloy development and laser surface melting

Mg-1Zn-2Dy (wt%) alloy was prepared by conventional casting route and which was achieved in a crucible made of mild steel with Ar + 2%SF_6 protective atmosphere. Initially Mg-Zn block was melted followed by addition of suitable amount of dysprosium (Dy) of 99.9% pure (Metal Industries, Mumbai) at 750 °C. Small amount of Zirconium (Zr-0.8 wt%) was added to the molten pool for grain refinement. To accomplish complete dissolution of the alloying elements (Dy, and Zn), the melt was subjected to stirring for 2 min and was held 20 min at 750 °C. Finally stirred melt was poured into a preheated (250 °C) rectangular mold (cast iron) of dimension 200 × 110 × 20 mm. IRIS INTREPID II XSP DUO, Thermo Electron, USA, Integrated Coupled Plasma-Atomic Emission spectroscopy (ICP-AES) was used to determine the chemical composition of the prepared Mg-Zn-Dy alloy. The nominal composition of developed alloy (in weight %) is 1 Zn, 1.9 Dy and

Table 1
Laser processing conditions and melt pool depth.

Laser power (W)	Laser velocity (mm/s)	Sample designation in terms of energy density (J/mm²)	Meltpool depth (μm)
125	10	25	150 ± 5
125	20	12.5	142 ± 5
175	10	35	100 ± 4
175	20	17.5	109 ± 4
225	10	45	98 ± 6
225	20	22.5	109 ± 6

balance Mg.

The Mg-Zn-Dy alloy block was cut into small rectangular samples with a dimension of 100 × 30 × 8 mm for laser surface melting. Prior to the laser melting these samples were prepared by polishing with different grades of abrasive polishing sheets (*SiC*) ranging from 100 to 2000 grit size. After fine polishing in velvet cloth with diamond paste (0.5 μm), all the samples are loaded to the machine glove box which is purged with argon gas before laser surface melting (LSM) process. Laser beam from MR7, Optomec Inc. USA (LENS™ machine) was employed for melting the surface of the Mg-Zn-Dy alloy. Ytterbium doped fiber laser with a beam diameter of 500 μm was used for laser melting. Different input laser powers (125, 175, 225 W) and velocities (10, 20 mm/s) were selected for laser melting. The equivalent energy densities were calculated by E = P/ν.d, where E = energy density (J/mm²), P = laser power (w), ν = scan velocity (mm/s) d = laser beam diameter (mm). Two consecutive laser scan where maintained at a distance of 0.5 mm. The laser processing conditions are listed out it in Table 1.

2.2. Microstructure, mechanical properties and phase analysis

The cross sectional microstructural and melt pool study was carried out by Scanning Electron Microscope (SEM) and Energy Dispersive Spectrum (EDS) (SU3500, HITACHI Japan). Different phase formation after LSM was determined using glancing X-Ray Diffractometer (XRD) (Rigaku smart lab, Japan). The as cast sample is further examined under TEM (JEM-2100, JEOL model) with an operating voltage of 200 kV. Samples were prepared initially by making a thin slice of 1 mm of the coupon using a slow speed precision cutting machine. Samples were subjected to mechanical thinning till 100 μm. Then, 3 mm discs were punched and dimpled to a thickness of about 4 μm at the center. Samples were then thinned to electron transparency by ion milling machine (PIPS II GATAN, USA) with an accelerating voltage of 5 kV and 5° gun angle. The micro-hardness of the cross sectional LSM samples were carried out using Vickers's micro hardness tester (Shimadzu HMV-G20, Japan) with an applied load of 25 g and a dwell time of 15 s. Average 10 measurements were taken for each processing conditions.

2.3. Surface roughness and wettability

To understand the surface topography changes with different laser processing conditions, Non-contact laser profilometer (OLYMPUS-LEXT OLS 4000, 3D laser measuring microscope, Japan) was used to understand the surface roughness of LSM and untreated surface. Defined surface area of 1 cm² was scanned for collecting Sq (root mean square height, μm) and S_a (Arithmetic mean height, μm) values.

Surface wettability of laser melted and polished Mg-Zn-Dy alloy samples were evaluated by static sessile drop technique (contact angle measurement). An average of three measurements was taken for better repeatability in the results. Effect of roughness on the wettability was analysed by conducting experiment on as processed LSM samples. In order to understand the effect of grain size and chemical composition on wettability, all LSM samples were polished to make identical surface roughness. DI water (polar) and diiodomethane (non-polar) liquid were

used to determine the surface energy by measuring the contact angles. Prior to the experiment all samples were cleaned in ultra-sonicator with alcohol. Liquid volume of 1 μL was dropped over the laser melted and polished samples. Goniometer attached with camera was used to capture the angle formed between the droplet of the liquid and sample surface. Fowkes equation [24] was used to calculate the surface energy of the sample surface.

2.4. In vitro degradation: immersion studies

In vitro degradation measurements were performed in a Hank's balanced salt solution (HBSS) (HIMEDIA, Labs, Bangalore) with an initial pH of 7.4. Specimen with an area of 1 cm^2 were mounted in the epoxy resin in such a way that LSM surface is allowed to expose to the electrolyte. It was reported that immersion corrosion studies is the most efficient technique to understand the Mg corrosion. It can be measured by three different ways (i) hydrogen evolution rate (2) ion (Mg^{2+}) release rate (iii) mass loss rate. The exposed surfaces were fine polished to avoid the roughness effect induced by the laser surface melting and it is further cleaned in ultrasonicator with ethanol. The weights of the samples before and after the experiment were measured using a high precision (0.0001) digital balance. The standard set up proposed by Song et.al [25] where an inverted glass funnel and burette were used to measure the hydrogen evolution at equal interval of time (every 24 h). Additionally, the corrosion rate through hydrogen evolution was calculated using following equations [25,26,27].

$$Pw = 3.65\Delta W/\rho \qquad (1)$$

where, P_w is the average corrosion rate in mm/year, ΔW is the weight loss rate of the sample in mg/cm^2 day and ρ is the density of the alloy.

The hydrogen evolution rate V_H (ml/cm^2 day) is related to ΔW (mg/cm^2 day) using the following relation:

$$\Delta W = 1.085 \, VH \qquad (2)$$

Finally the corrosion rate in mm/year from the hydrogen evolution rate was calculated by substituting the value of ΔW (Eq. (2)) in Eq. (1).

During immersion studies, 10 mL of solution (HBSS) was collected at every 24 h and Mg^{2+} ion release was measured using atomic absorption spectroscopy (932 plus, GBC scientific equipment Ltd., Australia). The pH and temperature were also monitored during the period of immersion.

All samples were taken out from the solution after the immersion test, and it is cleaned with a solution, containing 10 g/L silver nitrate and 200 g/L chromic acid, to eliminate the degradation products from the surface. The samples were washed with distilled water and ethanol then dried in warm air. After drying, the samples were weighed and the degradation rate was calculated using following relation, according to ASTM-G31-72 [28].

$$CR = \frac{K \cdot W}{D \cdot A \cdot T} \qquad (3)$$

where CR is the corrosion rate (mm/year (mmpy)), K is a constant (8.76 × 10^4 in millimetre per year), W is the variation in gram between the initial and the final mass of the sample, A is the area which is exposed (cm^2) to the solution, D is the density of the material in g/cm^3 and T is the total time of immersion (hours). The surface morphology and the degradation products of the immersed samples were examined using SEM, EDS (area mapping) and XRD.

3. Results and discussion

3.1. Microstructural characterization and phase analysis

Fig. 1 shows the SEM and TEM microstructures of Mg-1Zn-2Dy alloy in as cast condition. Fig. 1(a) indicates the major α-Mg matrix grains (dark in colour) and secondary phases distributed along the grain

boundaries in bright colour. The enlarged view in Fig. 1(b) shows that the secondary phase, in fact, is a eutectic phase (Mg$_8$ZnDy) and these hollow out Skelton structures are attached to long period stacking ordered structure (LPSO) [29]. The microstructure of the alloy was further analysed using TEM and Fig. 1(d) shows the presence of LPSO phase with lamellar morphology [30] having spacing between successive fringes of 0.97 nm. In addition Fig. 1(c), there are also some block shaped morphology reported as eutectic phase associated with LPSO formed along the α-Mg matrix grain boundaries, showing a discontinuous network morphology [31].

Fig. 2 shows the cross sectional microstructures of laser processed Mg-Zn-Dy at different laser energy density conditions. Compared to the substrate notable change in the microstructure was seen in the laser modified zone. In Fig. 2(a) the laser surface melted (LSM) zone was seen semi elliptical in geometry. There is a transition in the grain morphology from top to bottom of the laser melted zone. It seen in the Fig. 2(b) that the top portion of the laser melted zone resolidified as fine cellular grains, this refinement of grains mainly attributed to the high cooling rates associated in laser surface melting. While, the bottom portion of the specimen, Fig. 2(c), found to have columnar grains. This elongated grains mainly formed by the reduction in the solidification speed with increase in the depth of the LSM zone and there by directional heat extraction through the substrate. Remelting at lower energy density promoted the formation of micro cracks in the melt pool zone due to the changes in generated thermal stresses. The secondary phases (Mg$_8$ZnDy) present in the alloy were refined and distributed uniformly. The measured grain size of α-Mg in the laser melted zone was 2 μm which is very much lower than the substrate grain size of 60 μm. The changes in grain refinement and their magnitude are shown in Fig. 3. The highly refined zone (melt pool) processed at 25 J/mm^2 and 45 J/mm^2 are represented in Fig. 2(d) and (e). The depth of LSM region is an important factor that decides the life span of the components as the degradation due to corrosion starts from the surface penetrate through the thickness. Therefore, detailed assessment on variations in the melt pool depth as a function of laser process parameters was carried out and the results are shown in Table 1. Minimum melt pool depth of 98 μm was observed at 45 J/mm^2 and maximum depth of 150 μm was observed at 25 J/mm^2. At higher energy density the depth of the melt pool was decreased due more loss of material from the surface as a result of evaporation. At lower energy density condition comparatively continuous scan track with regular overlap of meltpool was observed. Apart from the power, scan speed significantly affects the meltpool morphology. When compared with the power and velocity changes on melt pool, the depth of the melt pool increases with increase in the velocity. In LSM the melt pool dimensions can be related to the following Eq. (4) [32].

$$I = \frac{Q}{V \times D} \qquad (4)$$

The total heat input (I) is related with laser power (Q), scan speed (V) and diameter of the laser beam (D). It can be seen that with increasing laser power the heat input increases, which increases the melt pool size. However, the experimental results do not follow this trend, Table 1, which is attributed to the partial evaporation of the alloy surface as a result of high melt pool temperatures generated at the meltpool due to higher resident time of laser beam at low scan velocities or high power [33]. The resident time of laser beam on the alloy surface can be illustrated by the ratio of laser beam diameter to scan velocity, which results in resident time for 10 mm/s and 20 mm/s are 0.5 s and 0.25 s respectively. So the partial evaporation of surface during the laser melting causes decrease in the meltpool depth. When the high intensity beam incident on the surface the localized melting and evaporation of material starts by absorbing the laser energy. The increased incident power generally increases the vaporization rate and marangoni flow by increasing the temperature in the meltpool [34]. When higher energy density 45 J/mm^2 applied on the surface at a
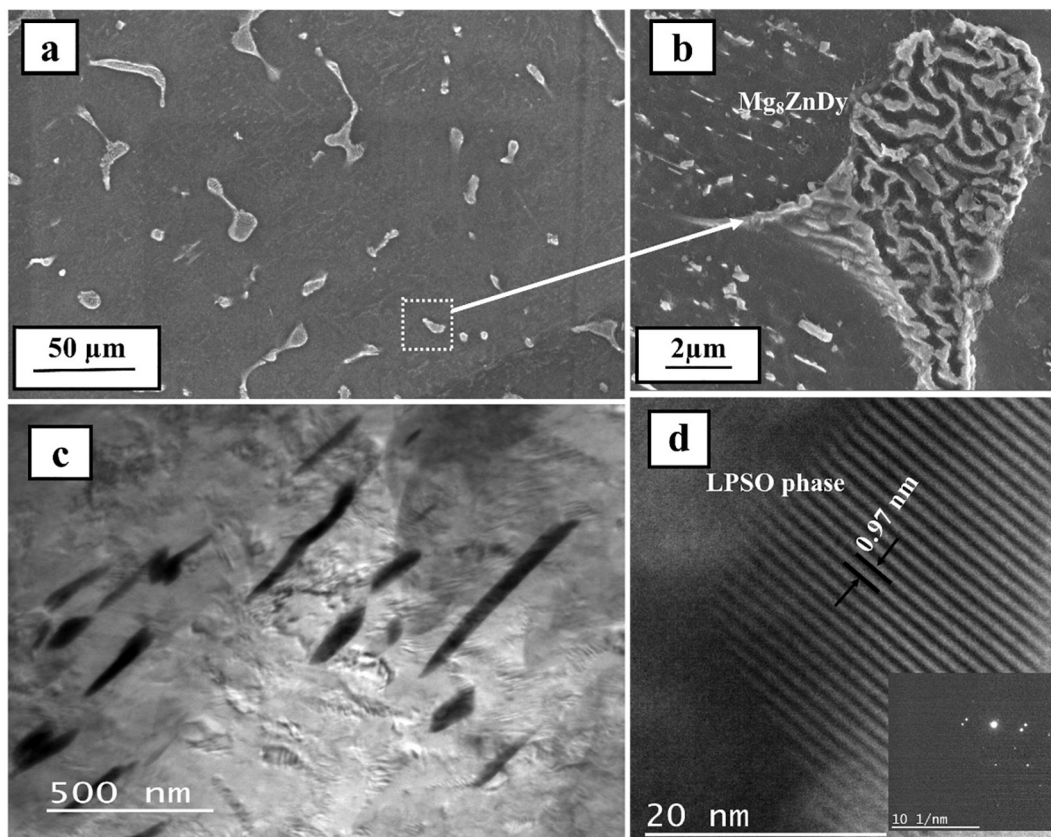
Fig. 1. SEM images showing the microstructures of (a) as cast Mg-Zn-Dy alloy (b) High-magnification image showing the eutectic phase, and TEM images of (c) Secondary phase (d) LPSO phase with SAED pattern.
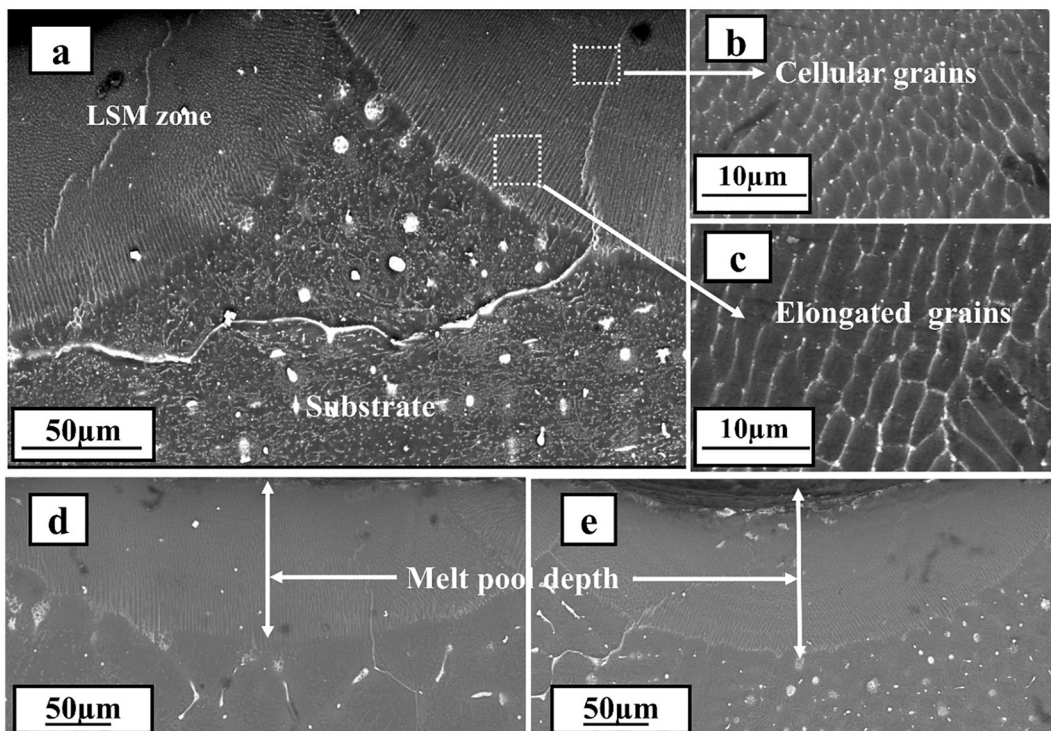

Fig. 2. Typical cross sectional microstructure of laser surface melted Mg-Zn-Dy (a) at 25 J/mm^2 (b) and (c) Enlarged view of microstructural changes in different regions (d) and (e) Meltpool depth of the alloy processed at 25 J/mm^2 and 45 J/mm^2 respectively.
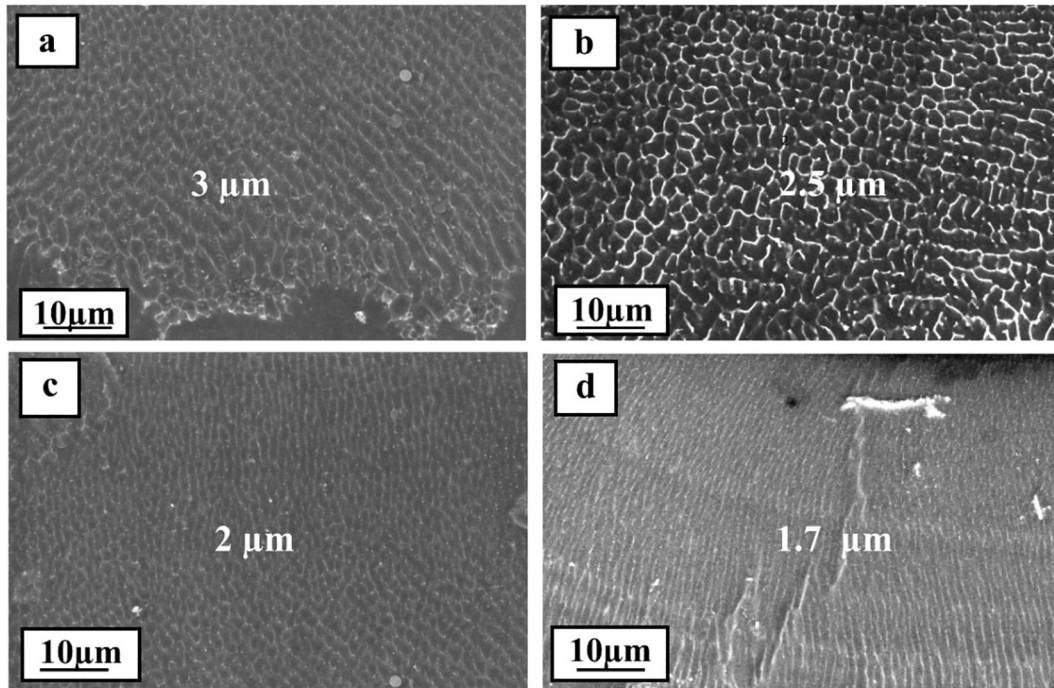
Fig. 3. SEM micrograph of LSM zone shows the grain refinement for (a) 12.5 J/mm^2 (b) 25 J/mm^2 (c) 35 J/mm^2 and (d) 45 J/mm^2 processed samples. The average grain size in μm is displayed on all the SEM images.

shorter incident time, it generates liquids to flow outwards to the pool edge in a greater extent. This makes the meltpool with a concave bottom with reduced depth at higher energy density [35].

During normal solidification of this alloy, the Dy atoms accumulate at solid/liquid junction due to their low solid solubility at low temperature and cannot diffuse away from the grain boundaries [36]. Therefore, the concentration of Dy within the grains of as cast alloy will be low. However, during LSM the rapid heating and cooling rates do not allow the solute atoms to diffuse or precipitate out during solidification [16] leading to the enrichment of Zn and Dy in the laser melted zone as shown in Table 2. Fig. 4 shows the point and line EDS analysis in the LSM zone of sample processed at 25 J/mm^2. In Fig. 4(a) point 1 indicates the spot analysis in the LSM zone. The corresponding elemental distribution is mapped in Fig. 4(a.1). An average of the weight percentage of the elements with standard deviation is documented in Table 2. Fig. 4(b) shows the line EDS analysis of the same sample in the LSM zone. The average elemental distribution is mapped in Fig. 4(b.1). Both the analysis (point and line) show the enrichment of Dy and Zn throughout the LSM zone at 25 J/mm^2. The elemental composition determined using EDS shows that the concentration of alloying elements is different in the melt pool compared to that in the substrate region. In the substrate the concentration of Dy is more in the eutectic structure present in the grain boundary than in the α-Mg matrix. The LSM zone EDS analysis confirms that there is no loss of alloying elements in the melt pool region. Moreover, the concentration of Dy in the LSM zone is relatively high, compared to substrate region, and could be

due to rapid cooling rates induced supersaturation of the liquid metal and potential evaporation of Mg during the laser melting [37] (Table 2).

Fig. 5 shows XRD patterns of as-cast and LSM samples at different energy densities. Apart from major α-Mg phase, all samples showed secondary phases corresponding to Mg$_7$Zn$_3$ and Mg$_8$ZnDy. It is seen that all samples show a dominant sharp peaks at 2θ = 32.19°, 34.4° and 36.63° which are indexed to (100) (002) and (101) planes, respectively, corresponds to α-Mg phase (JCPDF file no. 00-035-0821). It is also observed that the intensity of (101) peak increases with laser energy density while the other two dominant peaks (100) (002) get reduced, which implies some preferred grain orientation along (101) in LSM samples. The diffraction peaks at 2θ ranging from 40° to 80° shows additional peaks related to the formation of secondary intermetallic phases (Mg$_7$Zn$_3$ and Mg$_8$ZnDy) [36,38,18]. During laser melting, the concentration of Zn and Dy (Table 2 and Fig. 4) increased in the α-Mg matrix which leads to lattice parameters changes. The high concentration of these elements in the matrix is attributed to the loss of Mg due to evaporation and dissolution/disintegration in the concentration of intermetallic components in LSM samples [14]. The enrichment of Zn and Dy results to changes in the lattice parameter is observed in XRD plot. The diffraction peaks of lased melted samples gradually shifted towards higher scattering angles due to decrease in lattice parameter of α-Mg phase.

3.2. Microhardness and surface roughness

The effect of LSM on the hardness Mg-Zn-Dy alloy is presented in Fig. 6. The range of average hardness of present samples varied between 73 HV for as cast to 94 HV for LSM samples. The improvement in the hardness of LSM samples is due to grain refinement (shown in Fig. 3) and solid solution strengthening. When the laser energy was increased from 12.5 J/mm^2 to 35 J/mm^2 the hardness increased as a result of grain refinement (from 3 μm to 2 μm) in the melt pool. Maximum hardness of 94 HV was observed at 35 J/mm^2 due to refined grains and dendritic region of the Mg-Zn-Dy structure. However at 45 J/mm^2, the marginal decrease in hardness can be attributed to grain

Table 2
EDS analysis of melt pool region and substrate (as cast) of Mg-Zn-Dy alloy.

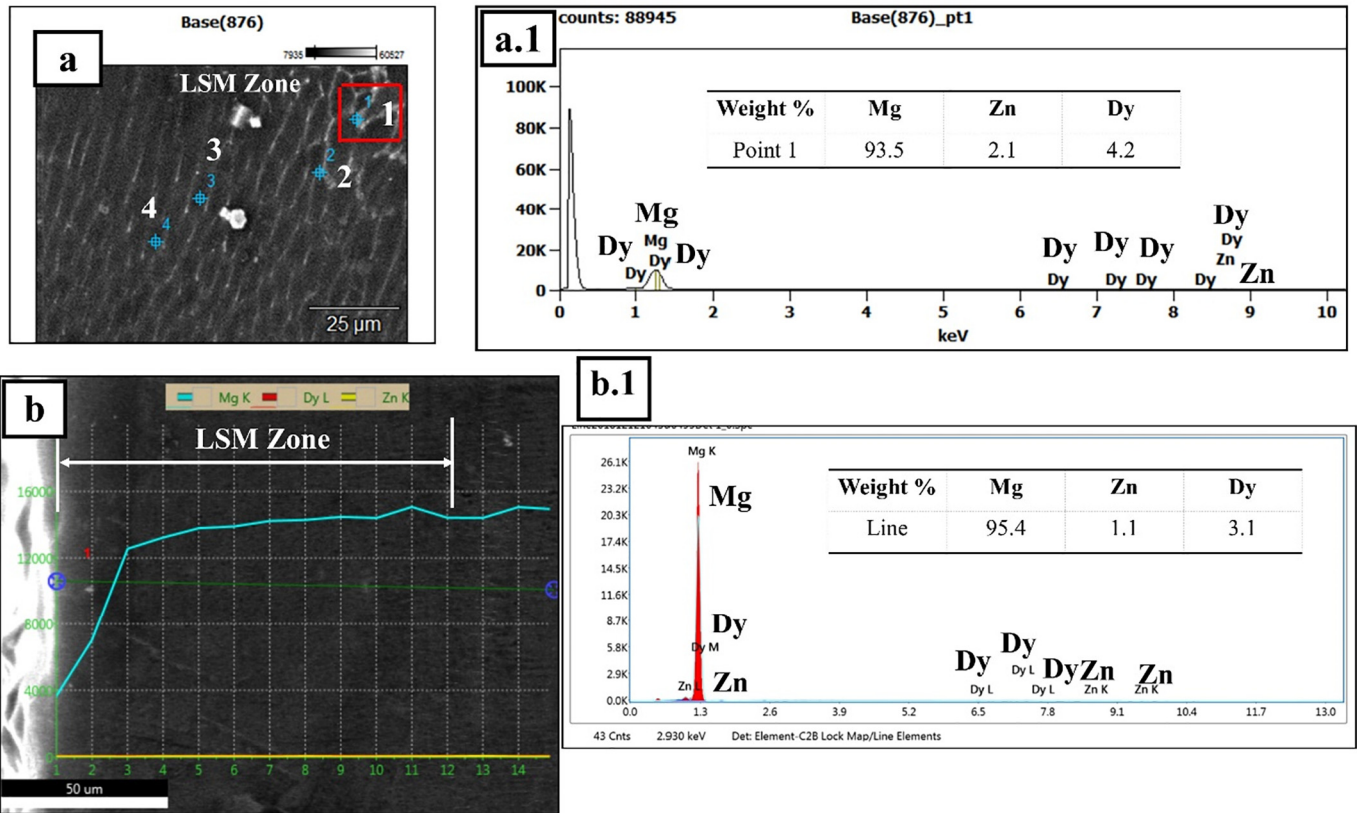| Alloy conditions (within the grain boundary)	Mg	Zn	Dy
	Weight percentage (%)		
As cast	93.5 ± 3	2.1 ± 2	3.2 ± 4
12.5 J/mm^2	92.9 ± 1	1.6 ± 0.4	5.4 ± 1
25 J/mm^2	91.2 ± 2	2.2 ± 1	6.2 ± 2
45 J/mm^2	88.0 ± 1	3.5 ± 0.5	8.4 ± 0.7

Fig. 4. EDS results of 25 J/mm^2 sample shows the elemental distribution through (a) point and (b) line analysis.
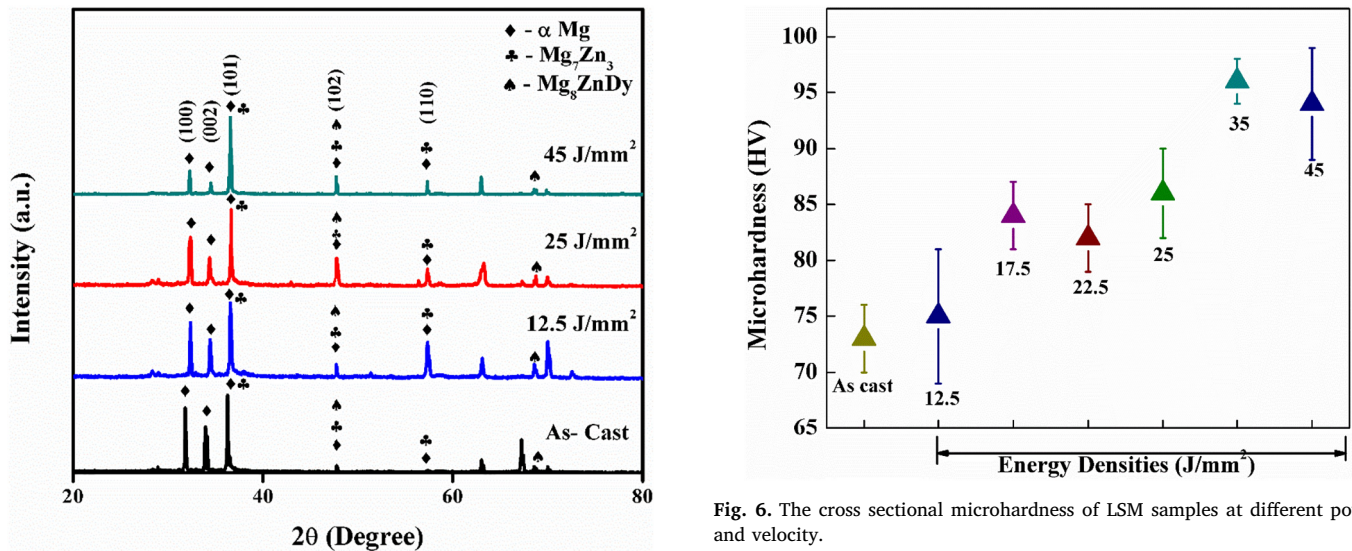

Fig. 5. X-Ray diffraction analysis of different phases in as cast and laser melted Mg-Zn-Dy alloy.

Fig. 6. The cross sectional microhardness of LSM samples at different power and velocity.

size variation at increased scan speed and similar trends have also been reported in literature [39].

The variation in the 3D surface roughness parameters of LSM processed Mg-Zn-Dy alloy is documented in Table 3 and shown in Fig. 7. The results of non-contact profilometer show an increase in the surface roughness with increase in laser energy density. Fig. 7(a) shows the general topography of the laser treated sample obtained using SEM. Fig. 7(b), (c) and (d) show the scanned area surface roughness profile of samples processed at 12.5 J/mm^2, 35 J/mm^2 and 45 J/mm^2 energy densities respectively. Surface roughness parameter (Sq) of LSM

samples varied between 3.9 ± 0.3 μm to 9.16 ± 0.9 μm, when the laser energy density was increased from 12.5 to 45 J/mm^2. The mechanism of evolution of different surface topography during laser processing is described by numerous researchers [18,40,41]. When the laser beam strikes on the alloy surface, the part of the energy being received by the material leads to the melting and the extent of melting primarily depends on laser processing parameters (in this study power and velocity) and material properties. The high energy density beam creates localized evaporation of the material. The evolved vapour from the melt zone (meltpool) creates a recoil pressure on the liquid melt zone. The consequence of recoil pressure is the generation of hydrodynamic melt motion and discharge of melt liquid towards the melt pool edges. Once the beam moves out from the interaction zone the liquid materials

Table 3
Surface roughness, surface energy and contact angles of laser melted and polished laser melted samples processed at different laser processing conditions.

Laser processing conditions	Surface roughness (Sq)	Laser melted		Laser melted and polished	
		Contact angle (°)	Surface energy (mN/m)	Contact angle (°)	Surface energy (mN/m)
As cast	1.4 ± 0.2	92 ± 2	12 ± 2	92 ± 2	17 ± 2
12.5	4.5 ± 0.3	70 ± 8	28 ± 5	64 ± 1	36 ± 1
17.5	3.9 ± 1	71 ± 7	22 ± 3	65 ± 2	34 ± 3
22.5	6.6 ± 0.2	74 ± 2	21 ± 3	72 ± 2	32 ± 2
25	7 ± 0.3	77 ± 7	19 ± 6	75 ± 2	31 ± 2
35	8.1 ± 0.5	80 ± 2	17 ± 2	79 ± 2	34 ± 2
45	8.7 ± 0.9	86 ± 10	15 ± 6	83 ± 2	32 ± 2

solidifies quickly because of higher cooling rate and self-quenching effect. This repeated instant heating and cooling process leads to a noticeable surface topography at different laser processing conditions. The increase in surface roughness with increase in laser power might be due to higher recoil pressure induced shock waves at the melt pool zone.

3.3. Wettability and surface energy behaviour

Wetting behaviour of as cast, LSM samples before and after polishing was carried out using two different liquids and the surface energy of samples determined using contact angles is shown in Table 3. The effect of surface roughness, microstructure and chemical composition on the wetting behaviour can be identified from the data of laser melted and polished samples. Usually contact angles < 90° indicates favourable wetting by spreading the fluid over large surface area. The contact angle of the samples was determined in laser melted condition to assess the overall change in the wettability. The samples processed at different

laser energy density showed different surface roughness, different microstructural features as well as few solute enrichment. So in order to assess how the microstructural and composition changes of the alloys influences the wettability due to laser melting, the sample surfaces have been polished to ensure similar roughness. Later the wettability has been assessed on these polished surfaces. The wettability of polished surfaces is expected to provide the influence of changes in the surface microstructure and composition on wettability. The results represented in Table 3 exhibits notable changes in contact angle and surface energy. The suitable hydrophilicity and surface energy obtained at energy densities of 22.5 and 25 J/mm^2, as the more recommended contact angle for biomedical implant is in the obtained range. Compared to as cast alloy grain size reduction has significantly happened in the order of 2 μm for laser melted samples and which is 90% less than the grain size of as cast alloy. The reduction in the average grain size with increasing energy density attributed by the increasing number of nucleation sites [18]. Further the large grain boundary area with grains at different orientation changes the contact angle. These grains and grain boundary could react to the DI water molecule differently. Consequently small grain with large grain boundary area lead to heterogeneous chemical composition [19]. EDS analysis confirms that distribution of elements (Mg, Zn, and Dy) chemical composition varies with different LSM processing parameters. The low wetting behaviour at higher energy density condition mainly due to the heterogeneous chemical composition of elements. Maximum surface energy of 36 mN/m at 12.5 J/mm^2 and minimum of 31 mN/m at 25 J/mm^2 were observed for polished samples (Table 3).

The laser melted samples showed superior wettability in terms of lower contact angles compared to as-cast alloy (Table 3). Further, the wettability appears to increase with laser energy density to an extent. It has been reported that better bone cell adhesion and its mineralization could be achieved with higher surface energy and lower contact angle [18]. As the value of contact angle increases from 70° to 86° in laser melted samples, the surface energy was found to decrease from 28 mN/m to 15 mN/m. At lower energy conditions, surfaces are hydrophilic in
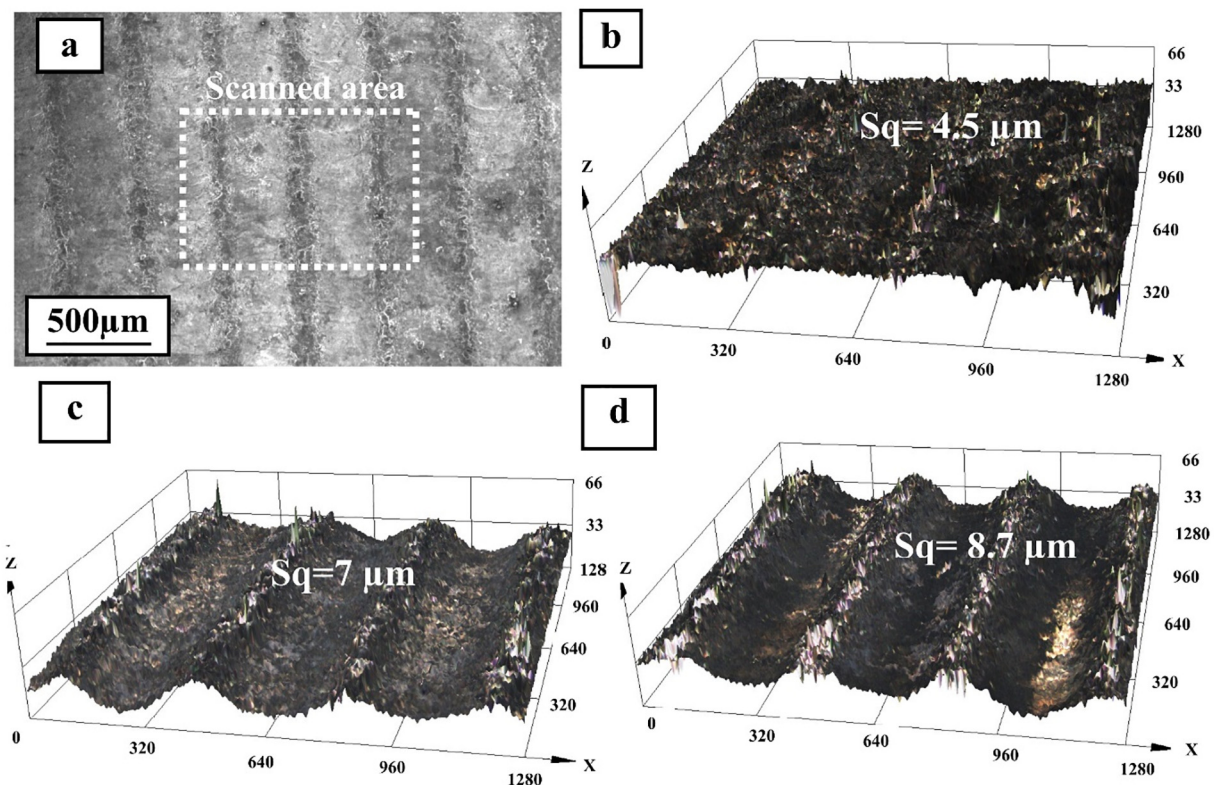

Fig. 7. Surface morphology of laser melted samples (a) SEM micrograph, 3D roughness profile of (b) 12.5 J/mm^2 (c) 25 J/mm^2 (d) 45 J/mm^2.

nature. But for the higher energy density condition (45 J/mm^2) surfaces exhibits nearly hydrophobic (86°) nature and this can led to poor cell attachment. Besides, the resulted surface energy of as cast alloy is 12 mN/m was very much lower than laser processed samples. The surface topography generated on this alloy due to laser melting is beneficial as it generally improves the cell adhesion and helps in osteointegration [19]. Suitable roughness at nano and micro-scales is a useful quantity that has been directly related to the wettability and surface energy [42]. Consequently, laser irradiated surface with hydrophilic nature presumably accelerated the wettability. The changes in the cooling rates and solidification rates at different energy densities corresponds to the changes in surface roughness [18]. As a result of laser processing, the surface roughness increased (Sq = 4.5 to 8.7 μm) with increasing energy density which eventually decreased the surface energy from 28 mN/m to 15 mN/m. The less valleys and radial grooves at lower roughness (~4.5 μm) would impede the scattering of water droplet at the laser meted sample surfaces. Similarly surfaces with more valleys and honed edges at higher surface roughness (8.7 μm) no longer efficient of keep the water droplets at higher energy density conditions. So the sample exhibit higher apparent contact angle (86°) which is almost close to hydrophobic in nature. Regarding the biomaterial surfaces wettability, cells tends to attach and proliferate effectively on surfaces with contact angle of around 70° [43,44]. Therefore, present LSM samples shows desirable degree of wettability and the results indicate that the surface roughness and related properties can be tailored by changing the laser processing parameters. The results showed that with respect to the nature of demand, the samples with roughness or without roughness can be considered for implant application.

3.4. In-vitro degradation

The degradation rate of laser melted Mg-Zn-Dy alloy and its kinetics were measured by weight loss, hydrogen evolution, magnesium ion (Mg^{2+}) release during the static immersion study in HBSS. All the laser melted as well as as-cast samples are fine polished to avoid the roughness effect on corrosion and maintained a Sq value of ~1 μm. The degradation rates of different samples are summarized in Table 4 and plotted in Fig. 9. The better degradation correlation is made with laser energy density and it is represented in graph without the unit for easy representation (e.g. 12.5 J/mm^2 as 12.5). Fig. 8(a) shows the amount of hydrogen evolution trend measured at every 24 h of time. It is observed that the hydrogen evolution gradually increasing in trend up to 140 h of immersion and later on it starts decreasing with increasing immersion time and similar kind of increasing trend has been observed in laser melted Mg-Zn-Gd alloy [45]. The rate of degradation is rapid in as cast alloy compared to laser melted samples. Out of all processing conditions, low energy density (12.5 J/mm^2) processed sample shows higher hydrogen evolution during the immersion (maximum value 0.7 mL/cm^2) time owing highest degradation rate. However after a period of immersion (~144 h) as cast and 12.5 J/mm^2 samples exhibits close matching in hydrogen evolution trace mainly attributed by stable passive film formation.

Table 4
Corrosion rate comparison through immersion studies.

As cast/LSM samples (J/mm^2)	Corrosion rates (mmpy)		
	Weight loss	Hydrogen evolution	Mg^{2+} ion release
As-cast	3.3 ± 0.1	2.5 ± 0.1	3.8 ± 0.8
25	2.6 ± 0.2	1.2 ± 0.3	2.3 ± 0.6
12.5	2.9 ± 0.5	2 ± 0.3	2.8 ± 0.5
35	2 ± 0.7	1 ± 0.2	2.2 ± 0.5
17.5	2.2 ± 0.6	1.3 ± 0.1	2 ± 0.7
45	0.9 ± 0.1	0.3 ± 0.1	1.2 ± 0.5
22.5	1.2 ± 0.3	0.6 ± 0.4	1.5 ± 0.8

The lower corrosion resistance at 12.5 J/mm^2 and 25 J/mm^2 conditions mainly due to the solidification crack during the laser melting process. It is seen that slopes of the curve is higher during the initial period of immersion (~ upto 96 h) represent higher hydrogen evolution rate for as cast, 12.5 and 25 J/mm^2 samples, and it is of order 0.004 mL/cm^2/h, 0.0042 mL/cm^2/h, 0.0038 mL/cm^2/h respectively. Further lower hydrogen evolution rate of 0.002 mL/cm^2/h is observed for 45 J/mm^2 processed sample. The moderate amount of hydrogen evolution was observed for 35 J/mm^2 sample and during the initial period of immersion the slope of trace steeper and later side (~120 h) there is a drastic reduction shows stable passive film formation. After 140 h of immersion in HBSS the release of hydrogen evolution gradually retards mainly assisted by the insoluble protective layer formation. The volume of hydrogen released in the implanted magnesium alloys should be carefully monitored. If the hydrogen gas evolved excessed in quantity than the hydrogen absorption capacity of the tissues which are surround to the implanted area may cause detachment of tissues and gas embolism [3].

The degradation process in HBSS solution also complimented by the anodic reaction (Mg→Mg^{2+} + 2e) and the cumulative release of Mg^{2+} ion observed is represented in the Fig. 8(b). With the increase in time of immersion the more of Mg^{2+} ions are dissolved into the solution. Studies reported that the release of Mg^{2+} retard the degradation because of magnesium containing precipitate (Mg^{2+} + 2OH$^-$→Mg (OH)$_2$) [46] formation on the surface of the samples. The observed ion release with respect to the immersion time found to match with the hydrogen evolution trend (Fig. 8(a)). During the initial period of immersion (~100 h) higher anodic dissolution leads to sharp increment in the ion release promotes higher degradation. At higher energy density condition (45 J/mm^2), the maximum ion release is 17 ppm and which is found to be less than the as cast sample of 23 ppm ion release. This higher The maximum possible Mg^{2+} ion release among the laser processed samples observed is 23.7 ppm for 12.5 J/mm^2 and after 144 h of immersion it offers an increase in ion release trend than as cast sample. It was documented that magnesium appeared in the orthopaedic implants could increase the sticking of osteoblastic cell [47]. Henceforth, magnesium could play a prominent role in the bone tissue growth.

The human body pH comparatively constant in between 7.35 and 7.45 [48]. Although there is possibility of pH fluctuation during the metabolic activity and there by release of hydrogen ions. It is also evident that after bone implantation pH value at the fracture site reaches as low as 5.5 during the recovery period [49]. So it is important to monitor change in pH during the immersion study to understand the mechanism of corrosion behaviour and bio-mineralization effectively for design of Mg based implants. Fig. 8(c) shows the change of the pH values of HBSS during the immersion study of samples. The typical increase in pH value observed for all samples. The change in pH value (< 11) leads to anodic dissolution of Mg and cathodic reaction of hydrogen reduction and (OH)$^-$ release [50]. It can be observed from the Fig. 8(c) there is a sharp increase in the pH curve for as cast Mg-Zn-Dy and 12.5 J/mm^2 samples during the immersion of 180 h. pH start raises from 7.4 and reaches to 8.5 for 12.5 J/mm^2 owing to higher degradation rate. The samples processed at higher energy densities (35, 45 J/mm^2) shows increase in pH during the initial period of immersion and become stable after 120 h of immersion. The decreased corrosion rate could be due to the accumulation of passive film in a larger dimension on the exposed surface. EDS analysis (Fig. 11(a)) also shows that products formed on these surface are mainly hydroxides and with a part of phosphates. The volume of hydrogen, Mg^{2+} ion released are also found to be small at higher energy density conditions as and its corrosion rates are determined. The change in pH is moderate for samples processed at 17.5 and 25 J/mm^2 and it reaches maximum pH of 8 during the immersion.

The mass loss, hydrogen evolution and Mg^{2+} ion release rates are now reworked in terms of corrosion rate and is represented in Table 4 and Fig. 9. The laser processed samples shows a significant
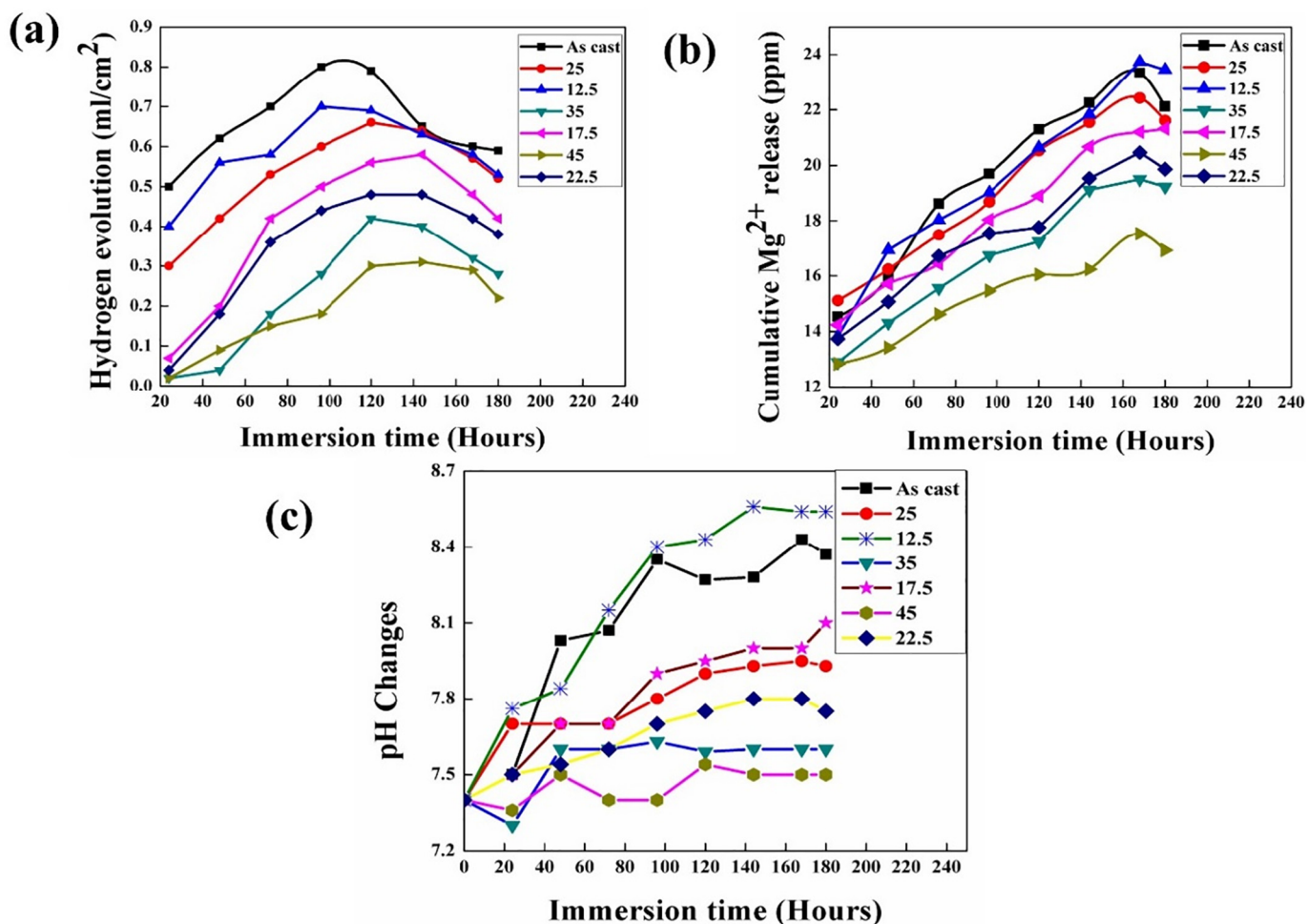
Fig. 8. (a) Hydrogen evolution (b) Mg^{2+} release and (c) pH changes are extracted during the immersion study in HBSS.
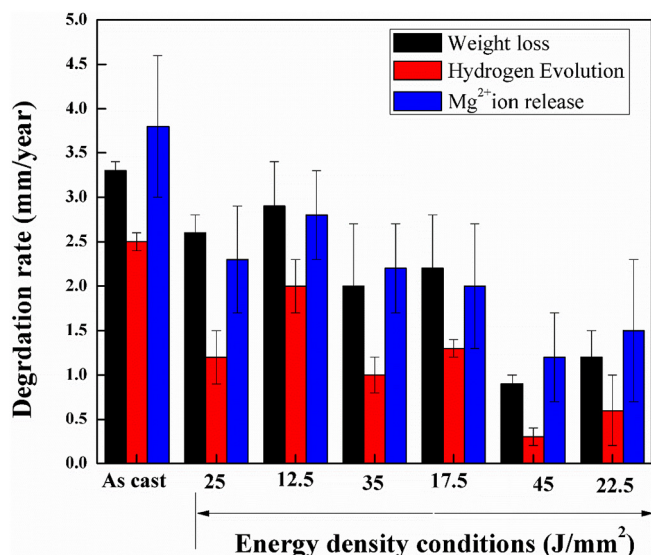

Fig. 9. Measured degradation rate and it comparison after 180 h of immersion in HBSS.

improvement in the *in-vitro* degradation rate except lower energy density conditions at all three ways of measurements. It is observed that there is a maximum of 72% improvement at 45 J/mm^2 (0.9 mmpy) laser processed sample as compared to as cast Mg-Zn-Dy (3.3 mmpy)

alloy through weight loss method. The trends of the obtained degradation rates from three different ways of calculations are in line with each other. The samples processed at 12.5 J/mm^2 shows higher degradation rate compared to other energy densities and as cast alloy mainly due to the formation of micro-crack at the meltpool and poor overlapping of successive meltpool (Fig. 10(d), (e)). These solidification crack will further act as a corrosion site for corrosion propagation. The advancement of corrosion also due to the corrosion potential between laser modified zone, HAZ (heat affected zone) and substrate. Moderate corrosion rate was observed for samples processed at 35 J/mm^2 and 17.5 J/mm^2. The degradation of the as cast Mg-Zn-Dy is mainly can happen by the formation of galvanic couple between the secondary phases and α-mg matrix. Additionally, the distribution and amount of secondary phases, morphology have great influences on degradation resistance [51]. The more finely and continuously distributed secondary phases dominated in the laser melted region helps in improving the degradation resistance. Melting predominantly refine the grains and distribution of secondary phases along the grain boundary. This smaller magnitude of grain refinement leads to higher grain boundary area and thereby decrease the anode to cathode area ratio [17]. Similar way, in this study remelting of the secondary phases at higher laser energy densities (35 and 45 J/mm^2) lessen the galvanic corrosion induced by the potential difference between the matrix and secondary phases. As a result of that occurrence of pitting corrosion limited and more continuous passive film formed during the degradation. However alloy treated with other lower energy conditions steadily react with the solution and leading to pitting mode of corrosion and discontinuous corrosion layer. Even if the higher energy density condition offers a
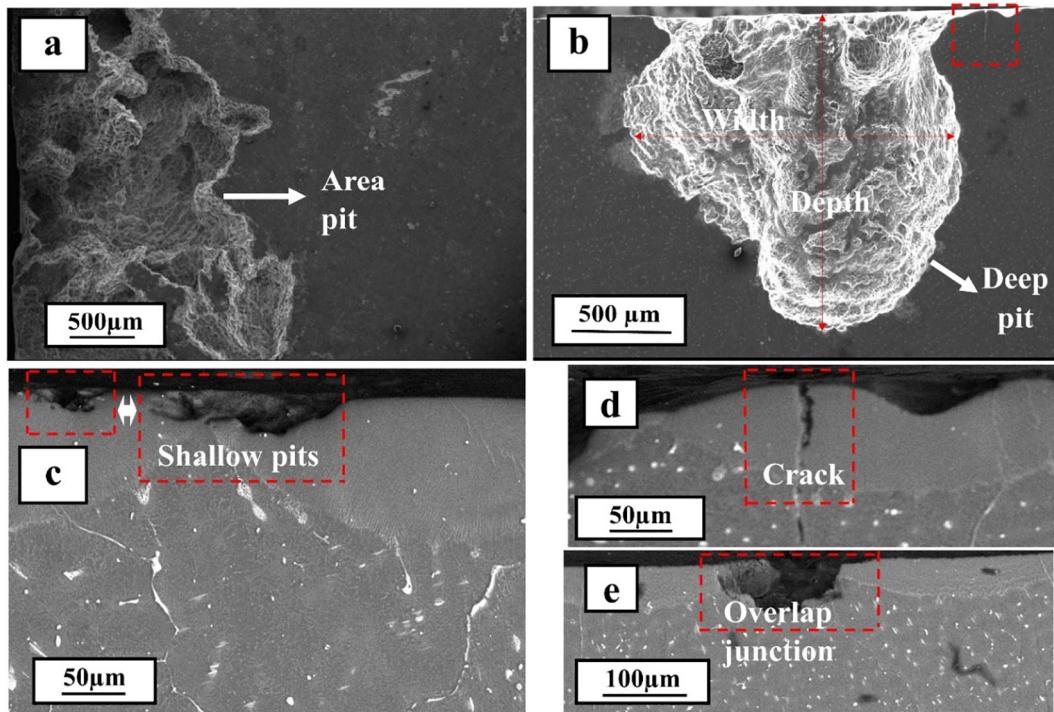
Fig. 10. SEM image of cross sections of samples after 180 h of immersion (a) As-cast sample (b) 12.5 J/mm² and (c) 45 J/mm² laser processed sample (d) Enlarged view of solidification crack (e) Pit at the overlapping zone.

better *in-vitro* degradation resistance during the 180 h of immersion, but due to the lower meltpool depth as compared to other density it is expected a lower the prolongation of modified surface with the exposed solution.

The behaviour of degradation is now observed with cross sectional and surface SEM images. The formation of products and its features are studied by EDS and XRD analysis. Fig. 10 shows the cross section SEM morphology of the samples after 180 h of immersion. Different magnification for the SEM images considered for the better understanding of corrosion mechanisms. For the as cast sample, (Fig. 10(a)) degradation followed by non-uniform distribution of secondary phases creating a large area of pit with corrosion product and in some area it reaches a maximum depth of 2.3 mm. The exposed surface of the sample in the Fig. 10(a) shows degradation is film form in nature for as cast alloy. In contrast to that laser melted samples showed lower degradation depth except the samples processed at 12.5 J/mm². Fig. 10(b) shows the samples with a pit of approximately 1.3 mm deep and 1.6 mm width, which is very much higher than the pits formed in the other laser processed samples and slightly closer to as cast samples. This higher rate of degradation observed mainly due to the solidification crack, which was clearly shown in Fig. 10(b) (marked with red colour) and enlarged at Fig. 10(d). However, in the case of 45 J/mm² the sample (Fig. 10(c)) is less affected with damage and by leaving a shallow pits at the meltpool zone. Fig. 11 describes the surface damages of the samples after the prolonged immersion. The degree of attack is considerably different in the as cast alloy samples. The corrosion reaction assumed to be start with localized pits and grows deeper and spread widely over the surface. This mechanism of movement of corrosion similar to filiform corrosion (Fig. 11(a)). It can be observed a visible pits in the Fig. 11(b) which are interconnected to the bulk material and results into sizeable holes leading the laser track to slightly peel off from the surface. After prolonged subjection of samples in the HBSS, 17.5 J/mm² samples localized pits are formed in the longitudinal direction (along the laser track) (Fig. 11(c)) and later in get progressed to the nearest laser track. It can also possible that due to the lower overlapping and coarse grain structure at the meltpool overlapping junction leading to constant pit

formation (Fig. 11(c)). At higher laser energy density conditions (35 J/mm² and 45 J/mm²), the localized degradation diminishes significantly leaving a shallow pits (Fig. 10(c)) and less corrosion products by leaving more pronounced area of laser tracks and (Fig. 11(d)).

The corrosion product which has formed after the long term immersion of the samples were highly stable and it is carefully scrapped off from the surface and studied in terms of bioactivity and corrosion resistance. The detailed analysis results are represented in the Fig. 12. It was reported that the necessary needs for a material to attach to living bone is the generation of bone like apatite once it is implanted in the body. So *in vivo* bone activity of new material can be evaluated by the apatite formation in HBSS. It was observed a discontinuous film formation with a large area of pit for as cast samples. Although, in laser processed samples continuous film with smaller dimension of pits. Fig. 12(a) shows the surface product morphology on the surface of the laser treated sample. Initially the formation of magnesium hydroxide $(Mg(OH)_2)$ precipitate at lower Mg^{2+} ion concentration [52] (higher energy density) permitting the existence of stable passive film on the surface and this protective layer formation is confirmed by XRD analysis(Fig. 12(c)). When the increase in pH there is a swift nucleation of HAp with concurrent formation of $Mg(OH)_2$. As the biodegradation proceeds the undissolved $Mg(OH)_2$ present on the surface of the alloy was also contemplated to bear feasible site for nucleation of hydroxyapatite by consuming the calcium (Ca) and phosphate ions from the HBSS [5]. The enlarged view (Fig. 12(a.1)) indicates the dense cluster structure (rod like structure) [53] with calcium and phosphorus enriched area similar to apatite formation. The XRD pattern of corrosion products showed a significant peaks of hydroxyapatite (HAp) at 2θ angle ranges from 18° to 70°, also showed that amount of formation of HAp is quiet dominant in the surface of the sample. Immersion study also resulted in the formation of calcium phosphate and it is indexed at 2θ of 28°, 38° for 25 J/mm² and 22°, 59°, 61° for 35 J/mm² samples. The elemental composition and mapping was examined and results shows that the surface mainly distributed with good amount of Ca, O, P, Mg and lower amount of Na and K. The average Ca/P ratio at different locations of the surface product is 1.6 ± 2 which is very close to the
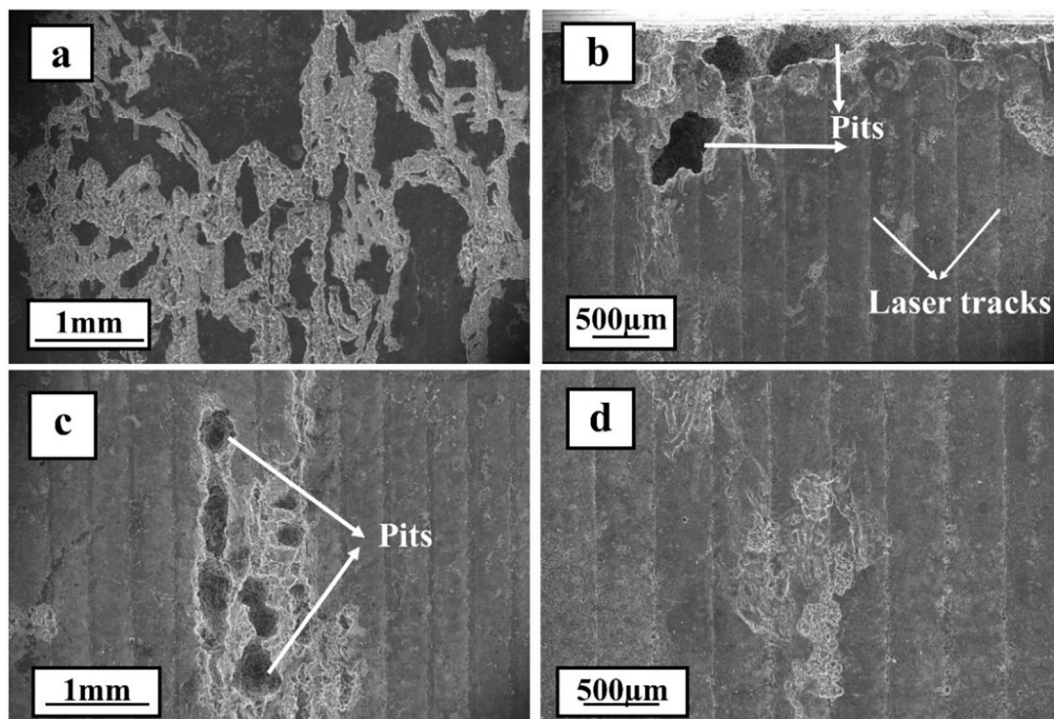
Fig. 11. SEM images of surface after 180 h of immersion at different magnification (a) as cast alloy (b) 12.5 J/mm^2 (c) 17.5 J/mm^2 and (d) 35 J/mm^2 laser processed samples.
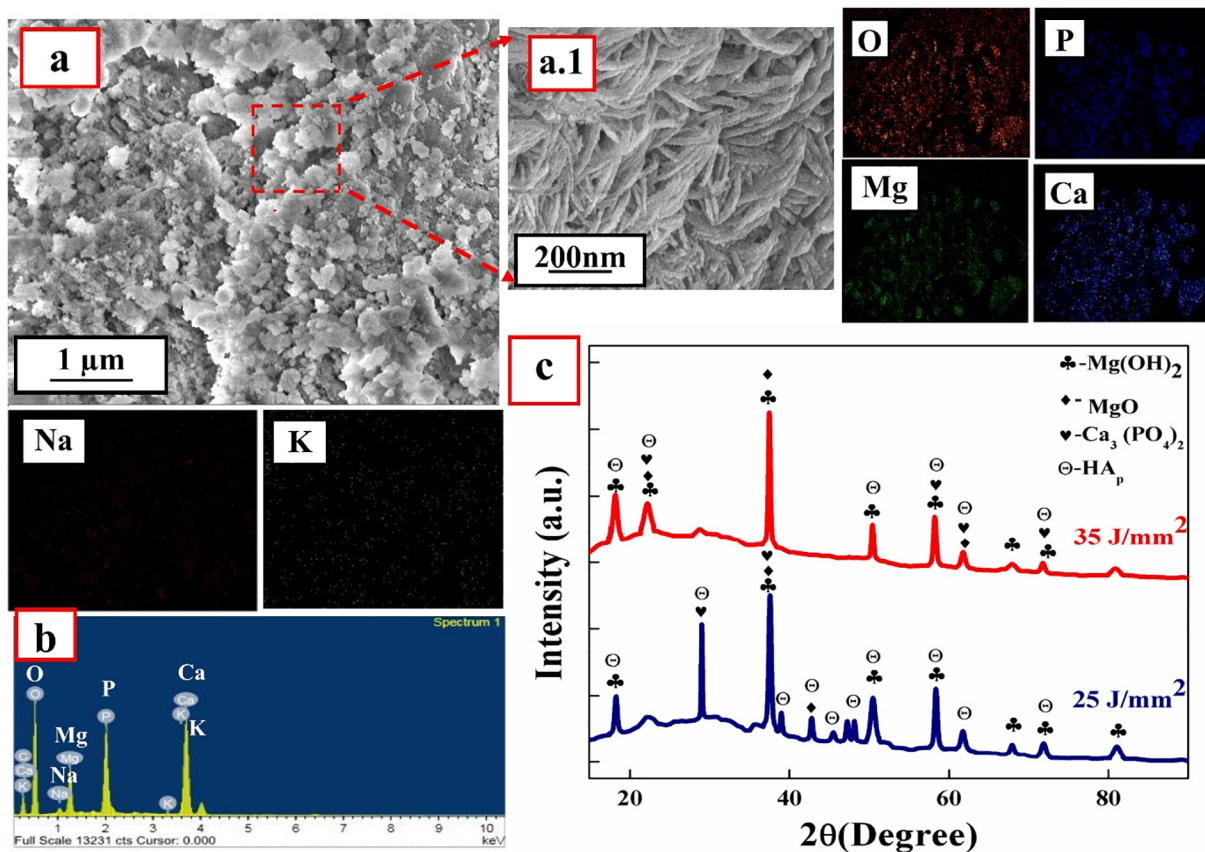

Fig. 12. SEM + EDS and XRD analysis of corrosion product.

stoichiometric ratio of Ca/P (1.67) [54] in HAp. The slight presence of carbon in the surface was due to the carbon dioxide dissolution [54].

4. Conclusions

It is investigated the laser surface melting on Mg-1Zn-2Dy alloy and based on the results following conclusions were drawn.

1. High degree of homogenisation with grain refinement in the range of microns was observed in the LSM region due to the rapid heating and cooling cycle. The increase in the laser energy density resulted in finer microstructures and the depth of melted region increased from 98 μm to 150 μm.
2. The wettability of the alloy was also improved due to LSM induced surface roughness, compositional and microstructural changes in the laser modified zones. As the energy density increases the surface roughness of the samples increased from 4.5 μm to 8.7 μm. The increase in surface roughness influences the surface energy and a maximum surface energy of 26 mN/m was observed at lower energy density (12.5 J/mm^2). However, in the case of laser melted and polished samples processed at the same energy density (12.5 J/mm^2), a surface energy value of 36 mN/m was observed.
3. The grain size reduction in the meltpool zone increases the grain boundary area and homogeneity of the chemical composition effectively improves the wettability.
4. *In vitro* degradation shows 72% (weight loss method) improvement in laser melted sample at 45 J/mm^2 as compared to as cast alloy.

Acknowledgments

References

[1] Y. Chen, Z. Xu, C. Smith, J. Sankar, Recent advances on the development of magnesium alloys for biodegradable implants, Acta Biomater. 10 (2014) 4561–4573, https://doi.org/10.1016/j.actbio.2014.07.005.

[2] K.U. Kainer, P. Bala Srinivasan, C. Blawert, W. Dietzel, Corrosion of magnesium and its alloys, Shreir's Corros. 51 (2010) 2011–2041, https://doi.org/10.1016/B978-044452787-5.00096-2.

[3] L.N. Zhang, Z.T. Hou, X. Ye, Z. Bin Xu, X.L. Bai, P. Shang, The effect of selected alloying elements additions on properties of Mg-based alloy as bioimplants: a literature review, Front. Mater. Sci. 7 (2013) 227–236, https://doi.org/10.1007/s11706-013-0210-z.

[4] S. Zhang, X. Zhang, C. Zhao, J. Li, Y. Song, C. Xie, H. Tao, Y. Zhang, Y. He, Y. Jiang, Y. Bian, Research on an Mg-Zn alloy as a degradable biomaterial, Acta Biomater. 6 (2010) 626–640, https://doi.org/10.1016/j.actbio.2009.06.028.

[5] Z. Li, X. Gu, S. Lou, Y. Zheng, The development of binary Mg-Ca alloys for use as biodegradable materials within bone, Biomaterials. 29 (2008) 1329–1344, https://doi.org/10.1016/j.biomaterials.2007.12.021.

[6] Y.C. Lee, A.K. Dahle, D.H. Stjohn, The Role of Solute in Grain Refinement of Magnesium, 31 (2000), pp. 2895–2906.

[7] F. Amerstorfer, S.F. Fischerauer, L. Fischer, J. Eichler, J. Draxler, A. Zitek, M. Meischel, E. Martinelli, T. Kraus, S. Hann, S.E. Stanzl-Tschegg, P.J. Uggowitzer, J.F. Löffler, A.M. Weinberg, T. Prohaska, Long-term in vivo degradation behavior and near-implant distribution of resorbed elements for magnesium alloys WZ21 and ZX50, Acta Biomater. 42 (2016) 440–450, https://doi.org/10.1016/j.actbio.2016.06.025.

[8] F. Feyerabend, J. Fischer, J. Holtz, F. Witte, R. Willumeit, H. Drücker, C. Vogt, N. Hort, Evaluation of short-term effects of rare earth and other elements used in magnesium alloys on primary cells and cell lines, Acta Biomater. 6 (2010) 1834–1842, https://doi.org/10.1016/j.actbio.2009.09.024.

[9] Z. Leng, J. Zhang, M. Zhang, X. Liu, H. Zhan, R. Wu, Microstructure and high mechanical properties of Mg – 9RY – 4Zn (RY: Y-rich misch metal) alloy with long period stacking ordered phase, Mater. Sci. Eng. A 540 (2012) 38–45, https://doi.org/10.1016/j.msea.2012.01.057.

[10] K. Hagihara, N. Yokotani, Y. Umakoshi, Intermetallics plastic deformation behavior of Mg 12 YZn with 18R long-period stacking ordered structure, Intermetallics. 18 (2010) 267–276, https://doi.org/10.1016/j.intermet.2009.07.014.

[11] H. Hornberger, S. Virtanen, A.R. Boccaccini, Biomedical coatings on magnesium alloys - a review, Acta Biomater. 8 (2012) 2442–2455, https://doi.org/10.1016/j.actbio.2012.04.012.

[12] J.E. Gray, B. Luan, Protective coatings on magnesium and its alloys — a critical review, J. Alloys Compd. 336 (2002) 88–113, https://doi.org/10.1016/S0925-8388(01)01899-0.

[13] A.E. Coy, F. Viejo, Z. Liu, P. Skeldon, G.E. Thompson, Effect of excimer laser surface melting on the microstructure and corrosion performance of the die cast AZ91D magnesium alloy, Corros. Sci. 52 (2010) 387–397, https://doi.org/10.1016/j.corsci.2009.09.025.

[14] C. Liu, J. Liang, J. Zhou, L. Wang, Q. Li, Effect of laser surface melting on microstructure and corrosion characteristics of AM60B magnesium alloy, Appl. Surf. Sci. 343 (2015) 133–140, https://doi.org/10.1016/j.apsusc.2015.03.067.

[15] G. Abbas, Z. Liu, P. Skeldon, Corrosion behaviour of laser-melted magnesium alloys, Appl. Surf. Sci. 247 (2005) 347–353, https://doi.org/10.1016/j.apsusc.2005.01.169.

[16] C. Taltavull, B. Torres, A.J. Lopez, P. Rodrigo, E. Otero, A. Atrens, J. Rams, Corrosion behaviour of laser surface melted magnesium alloy AZ91D, Mater. Des. 57 (2014) 40–50, https://doi.org/10.1016/j.matdes.2013.12.069.

[17] J. Dutta Majumdar, R. Galun, B.L. Mordike, I. Manna, Effect of laser surface melting on corrosion and wear resistance of a commercial magnesium alloy, Mater. Sci. Eng. A 361 (2003) 119–129, https://doi.org/10.1016/S0921-5093(03)00519-7.

[18] Y.H. Ho, H.D. Vora, N.B. Dahotre, Laser surface modification of AZ31B-Mg alloy for bio-wettability, J. Biomater. Appl. 29 (2015) 915–928, https://doi.org/10.1177/0885328214551156.

[19] J.I. Rosales-Leal, M.A. Rodríguez-Valverde, G. Mazzaglia, P.J. Ramón-Torregrosa, L. Díaz-Rodríguez, O. García-Martínez, M. Vallecillo-Capilla, C. Ruiz, M.A. Cabrerizo-Vílchez, Effect of roughness, wettability and morphology of engineered titanium surfaces on osteoblast-like cell adhesion, Colloids Surf. A Physicochem. Eng. Asp. 365 (2010) 222–229, https://doi.org/10.1016/j.colsurfa.2009.12.017.

[20] S.R. Paital, N.B. Dahotre, Wettability and kinetics of hydroxyapatite precipitation on a laser-textured Ca-P bioceramic coating, Acta Biomater. 5 (2009) 2763–2772, https://doi.org/10.1016/j.actbio.2009.03.004.

[21] S.N. Dahotre, H.D. Vora, R.S. Rajamure, L. Huang, R. Banerjee, W. He, N.B. Dahotre, Laser induced nitrogen enhanced titanium surfaces for improved osseo-integration, Ann. Biomed. Eng. 42 (2014) 50–61, https://doi.org/10.1007/s10439-013-0898-z.

[22] J. Lincks, B.D. Boyan, C.R. Blanchard, C.H. Lohmann, Y. Liu, D.L. Cochran, D.D. Dean, Z. Schwartz, Response of MG63 osteoblast-like cells to titanium and titanium alloy is dependent on surface roughness and composition, Biomater. Silver Jubil. Compend. 19 (2006) 147–160, https://doi.org/10.1016/B978-008045154-1.50019-8.

[23] A.G. Demir, V. Furlan, N. Lecis, B. Previtali, Laser surface structuring of AZ31 Mg alloy for controlled wettability, Biointerphases 9 (2014) 029009, , https://doi.org/10.1116/1.4868240.

[24] D.K. Owens, R.C. Wendt, Estimation of the surface free energy of polymers, J. Appl. Polym. Sci. 13 (1969) 1741–1747, https://doi.org/10.1002/app.1969.070130815.

[25] G. Song, A. Atrens, D. StJohn, An hydrogen evolution method for the estimation of the corrosion rate of magnesium alloys, Magnes. Technol. 2013 (2001) 254–262, https://doi.org/10.1002/9781118805497.ch44.

[26] Z. Shi, M. Liu, A. Atrens, Measurement of the corrosion rate of magnesium alloys using Tafel extrapolation, Corros. Sci. 52 (2010) 579–588, https://doi.org/10.1016/j.corsci.2009.10.016.

[27] A. Atrens, M. Liu, N.I. Zainal Abidin, Corrosion mechanism applicable to biodegradable magnesium implants, Mater. Sci. Eng. B 176 (2011) 1609–1636, https://doi.org/10.1016/j.mseb.2010.12.017.

[28] E. Cor, Standard practice for laboratory immersion corrosion testing of metals 1, Corrosion 72 (2004) 1–8, https://doi.org/10.1520/G0031-72R04.

[29] J. Zhang, C. Xin, K. Nie, W. Cheng, H. Wang, C. Xu, Materials science & engineering a microstructure and mechanical properties of Mg – Zn – Dy – Zr alloy with long-period stacking ordered phases by heat treatments and ECAP process, Mater. Sci. Eng. A 611 (2014) 108–113, https://doi.org/10.1016/j.msea.2014.05.067.

[30] J. Zhang, C. Xin, W. Cheng, L. Bian, H. Wang, C. Xu, Research on long-period-stacking-ordered phase in Mg-Zn-Dy-Zr alloy, J. Alloys Compd. 558 (2013) 195–202, https://doi.org/10.1016/j.jallcom.2012.12.165.

[31] S. Huang, J. Wang, F. Hou, X. Huang, F. Pan, Materials Science & Engineering A Effect of Gd and Y Contents on the Microstructural Evolution of Long Period Stacking Ordered Phase and the Corresponding Mechanical Properties in Mg – Gd – Y – Zn – Mn Alloys, 612 (2014), pp. 363–370.

[32] V.K. Balla, A. Bandyopadhyay, Laser processing of Fe-based bulk amorphous alloy, Surf. Coat. Technol. 205 (2010) 2661–2667, https://doi.org/10.1016/j.surfcoat.2010.10.029.

[33] B. Manne, H. Thiruvayapati, S. Bontha, R. Motagondanahalli Rangarasaiah, M. Das, V.K. Balla, Surface design of Mg-Zn alloy temporary orthopaedic implants: tailoring wettability and biodegradability using laser surface melting, Surf. Coat. Technol. 347 (2018) 337–349, https://doi.org/10.1016/j.surfcoat.2018.05.017.

[34] H.D. Vora, S. Santhanakrishnan, S.P. Harimkar, S.K.S. Boetcher, N.B. Dahotre, Evolution of Surface Topography in One-dimensional Laser Machining of, 32 (2012), pp. 4205–4218.

[35] B. Fotovvati, S.F. Wayne, G. Lewis, E. Asadi, A review on melt-pool characteristics in laser welding of metals, Adv. Mater. Sci. Eng. 2018 (2018), https://doi.org/10.1155/2018/4920718.

[36] B.I. Guangli, J. Jing, Z. Fan, F. Daqing, Microstructure Evolution and Corrosion Properties of Mg-Dy-Zn Alloy During Cooling After Solution Treatment, 34 (2016), pp. 931–937, https://doi.org/10.1016/S1002-0721(16)60117-5.

[37] Y.C. Guan, W. Zhou, H.Y. Zheng, Effect of laser surface melting on corrosion

behaviour of AZ91D Mg alloy in simulated-modified body fluid, J. Appl. Electrochem. 39 (2009) 1457–1464, https://doi.org/10.1007/s10800-009-9825-2.

[38] J. Zhang, C. Xin, K. Nie, W. Cheng, H. Wang, C. Xu, Microstructure and mechanical properties of Mg-Zn-Dy-Zr alloy with long-period stacking ordered phases by heat treatments and ECAP process, Mater. Sci. Eng. A 611 (2014) 108–113, https://doi.org/10.1016/j.msea.2014.05.067.

[39] K.R. Rakesh, S. Bontha, M.R. Ramesh, S.B. Arya, M. Das, Laser Surface Modification of Mg-Zn-Gd Alloy: Microstructural, Wettability and in Vitro Degradation Aspects Laser Surface Modification of Mg-Zn-Gd Alloy: Microstructural, Wettability and In Vitro Degradation Aspects, (2018).

[40] H.D. Vora, S. Santhanakrishnan, S.P. Harimkar, S.K.S. Boetcher, N.B. Dahotre, One-dimensional multipulse laser machining of structural alumina: evolution of surface topography, Int. J. Adv. Manuf. Technol. 68 (2013) 69–83, https://doi.org/10.1007/s00170-012-4709-8.

[41] V. Semak, A. Matsunawa, The role of recoil pressure in energy balance during laser materials processing, J. Phys. D. Appl. Phys. 30 (1999) 2541–2552, https://doi.org/10.1088/0022-3727/30/18/008.

[42] X. Zhu, J. Chen, L. Scheideler, R. Reichl, J. Geis-gerstorfer, Effects of Topography and Composition of Titanium Surface Oxides on Osteoblast Responses, 25 (2004), pp. 4087–4103, https://doi.org/10.1016/j.biomaterials.2003.11.011.

[43] Y. Arima, H. Iwata, Effect of wettability and surface functional groups on protein adsorption and cell adhesion using well-defined mixed self-assembled monolayers, Biomaterials. 28 (2007) 3074–3082, https://doi.org/10.1016/j.biomaterials.2007.03.013.

[44] J. Wei, T. Igarashi, N. Okumori, T. Igarashi, T. Maetani, B. Liu, M. Yoshinari, Influence of surface wettability on competitive protein adsorption and initial attachment of osteoblasts, Biomed. Mater. 4 (2009), https://doi.org/10.1088/1748-6041/4/4/045002.

[45] K.R. Rakesh, S. Bontha, M.R. Ramesh, S.B. Arya, M. Das, Laser surface modification of Mg-Zn-Gd alloy: microstructural, wettability and in vitro degradation aspects laser surface modi fi cation of Mg-Zn-Gd alloy: microstructural, wettability and in

vitro degradation aspects, Mater. Res. Express 5 (2018) 126502, , https://doi.org/10.1088/2053-1591/aadec6.

[46] F. Witte, F. Feyerabend, P. Maier, J. Fischer, M. Störmer, C. Blawert, W. Dietzel, N. Hort, Biodegradable magnesium-hydroxyapatite metal matrix composites, Biomaterials. 28 (2007) 2163–2174, https://doi.org/10.1016/j.biomaterials.2006.12.027.

[47] H. Zreiqat, C.R. Howlett, A. Zannettino, P. Evans, G. Schulze-Tanzil, C. Knabe, M. Shakibaei, Mechanisms of magnesium-stimulated adhesion of osteoblastic cells to commonly used orthopaedic implants, J. Biomed. Mater. Res. 62 (2002) 175–184, https://doi.org/10.1002/jbm.10270.

[48] P. Woodrow, Arterial blood gas analysis, Nurs. Stand. 18 (2004) 45–52 quiz 54-55 https://doi.org/10.7748/ns2004.02.18.21.45.c3544.

[49] W.F. Ng, K.Y. Chiu, F.T. Cheng, Effect of pH on the in vitro corrosion rate of magnesium degradable implant material, Mater. Sci. Eng. C 30 (2010) 898–903, https://doi.org/10.1016/j.msec.2010.04.003.

[50] H. Pan, H. Yang, X. Tang, J. Niu, Z. Xiang, Y. Song, W. Lu, Effect of Ca/P ratio on the structural and corrosion properties of biomimetic Ca[sbnd]P coatings on ZK60 magnesium alloy, Mater. Sci. Eng. C 72 (2017) 676–681, https://doi.org/10.1016/j.msec.2016.11.132.

[51] G. Song, S. Song, A possible biodegradable magnesium implant material, Adv. Eng. Mater. 9 (2007) 298–302, https://doi.org/10.1002/adem.200600252.

[52] S. Johnston, Z. Shi, A. Atrens, The influence of pH on the corrosion rate of high-purity Mg, AZ91 and ZE41 in bicarbonate buffered Hanks' solution, Corros. Sci. 101 (2015) 182–192, https://doi.org/10.1016/j.corsci.2015.09.018.

[53] H. Yang, H. Zeng, L. Hao, N. Zhao, C. Du, H. Liao, Y. Wang, Effects of hydroxyapatite microparticle morphology on bone mesenchymal stem cell behavior, J. Mater. Chem. B 2 (2014) 4703–4710, https://doi.org/10.1039/c4tb00424h.

[54] H. Yang, K. Xia, T. Wang, J. Niu, Y. Song, Z. Xiong, K. Zheng, S. Wei, W. Lu, Growth, in vitro biodegradation and cytocompatibility properties of nano-hydroxyapatite coatings on biodegradable magnesium alloys, J. Alloys Compd. 672 (2016) 366–373, https://doi.org/10.1016/j.jallcom.2016.02.156.